

Scaling of turbulence intensity for low-speed flow in smooth pipes



Francesco Russo^a, Nils T. Basse^{b,*}

^a Delft University of Technology, Faculty of Aerospace Engineering, Kluyverweg 1, 2629 HS Delft, The Netherlands

^b Siemens A/S, Flow Instruments, Coriolisvej 1, 6400 Sønderborg, Denmark

ARTICLE INFO

Keywords:

Flowmeters
Turbulence intensity scaling
Flow in smooth pipes
Incompressible and compressible flow
Princeton Superpipe measurements
Semi-empirical modelling
CFD simulations

ABSTRACT

In this paper, we compare measured, modelled, and simulated mean velocity profiles. Smooth pipe flow simulations are performed for both incompressible (below Mach 0.2) and compressible (below Mach 0.1) fluids. The compressible simulations align most closely with the measurements. The simulations are subsequently used to make scaling formulae of the turbulence intensity as a function of the Reynolds number. These scaling expressions are compared to scaling derived from measurements. Finally, the found compressible scaling laws are used as an example to show how the flow noise in a flowmeter is expected to scale with the mean flow velocity.

1. Introduction

Pipe flow noise is generated by turbulent fluid motion. For flowmeter manufacturers, it is important to understand and quantify pipe flow noise since it impacts the measurement performance, i.e. repeatability.

Reviews of wall-bounded turbulent flows at high Reynolds numbers are presented in [1,2]. For an overview of the logarithmic region of wall turbulence see [3]: here it is shown that the logarithmic mean velocity profile is accompanied by a corresponding logarithmic streamwise Reynolds stress profile.

From an engineering point of view, a scaling law is sufficient for most applications – for example, the turbulence intensity (TI) I [4] as a function of the Reynolds number Re . However, we have so far not been able to find well-documented scaling formulae of this kind. The only formula we have encountered is from the CFD-Wiki of CFD Online [5]. Here, the scaling on the axis of a pipe is provided as:

$$I_{\text{CFD-Wiki,pipe axis}} = 0.16 \times Re^{-\frac{1}{8}} \quad (1)$$

However, because no reference is provided for this formula, it is impossible to know the origin of the equation. That is the motivation for this paper: the purpose is to provide scaling formulae based on measurements, modelling and computational fluid dynamics (CFD) simulations [6]. To our knowledge, this paper is the first to document the scaling behaviour of I with Re found using both measurements and simulations.

Our paper is structured as follows: in Section 2, we introduce the mean velocity profile measurements used, followed by semi-empirical

modelling (SEM) in Section 3. CFD simulations are described in Section 4. The measured, modelled, and simulated mean velocity profile can be found in Section 5, and the corresponding simulated TI is compared to the measured TI in Section 6. An application example is found in Section 7. Finally, our conclusions are in Section 8.

Throughout the paper, we distinguish between incompressible and compressible flow, where possible. Based on CFD, we derive separate scaling formulae for these two cases.

2. Measurements

The Princeton Superpipe is documented in [7]. Measurements of the mean velocity profile were published in [8,9], and corrected measurements in [10]. We use the McKeon measurements, which are publicly available from [11].

The experiments were performed for a broad range of Re : from 7.4×10^4 to 3.6×10^7 . High Re were achieved using compressed air at ambient temperatures. Specifically, the static pressure went from one atm to 177 atm while the variation of the temperature was from 293 K to 298 K. The test section had a nominal diameter d of 0.129 m and a length L of 202 pipe diameters, which ensured a fully developed velocity profile in the test sections.

The inner wall of the pipe is considered to be hydrodynamically smooth for all Re , with a root-mean-square (RMS) roughness k_{RMS} of $0.15 \pm 0.03 \mu\text{m}$ [9]. This corresponds to a sand-grain roughness $k_s \approx 3k_{\text{RMS}}$.

Our objective in this paper is to derive scaling for smooth pipes. Therefore, most SEM and all CFD simulations below are made for a

* Corresponding author.

E-mail address: nilsbasse@npb.dk (N.T. Basse).

smooth pipe, i.e. with zero wall roughness.

3. Semi-empirical modelling

For SEM of the mean velocity profile, we use the formulation by Gersten [12]. Specifically, Eq. (1.55) is used for the mean velocity profile and Eq. (1.77) for the (Darcy) friction factor.

The mean flow velocity for cylindrical coordinates (r, θ, z) is defined as:

$$v_m = \frac{\int_A v(r, \theta) dA}{A}, \quad (2)$$

where A is the pipe cross-sectional area, v is the mean flow velocity profile, and flow is along the z direction. For pipe radius a , $A = a^2\pi$. For axisymmetric flow, the profile is independent of angle, i.e. $v(r, \theta) = v(r)$. Then we can rewrite Eq. (2) to:

$$v_m = \frac{\int_0^{2\pi} d\theta \int_0^a v(r) r dr}{a^2\pi} = \frac{2}{a^2} \times \int_0^a v(r) r dr \quad (3)$$

A comparison between the measured and modelled mean flow velocity profile for two v_m is shown in Fig. 1. At low velocity, the profile is more peaked than for high velocity.

To study differences between measured and modelled velocity profiles in more detail we can plot their ratio. See Fig. 2:

$$r_{v, \text{Model/Measurement}}(r) = \frac{v_{\text{Model}}(r)}{v_{\text{Measurement}}(r)} \quad (4)$$

For low velocity, the model underestimates the velocity in the core and overestimates the velocity closer to the wall. Agreement between the profiles is better for high velocity, i.e. $r_{v, \text{Model/Measurement}}(r)$ is closer to one.

To represent the deviation of the modelled from the measured profile, we define the modelled shape error (in percent) as:

$$E_{s, \text{Model/Measurement}} = 100 \times \frac{\sum_r |1 - r_{v, \text{Model/Measurement}}(r)|}{N}, \quad (5)$$

where N is the number of radial points, see Fig. 3. The variation of the modelled shape error with Re can be found in Table 1. For reference, we have also included the modelled profile with a rough wall using $k_s = 0.45 \mu\text{m}$ [9] in this table.

The data from Table 1 is shown in Fig. 4. The shape error becomes smaller with increasing Re up to 1×10^6 . The shape error is, generally speaking, somewhat lower for high Re when roughness is included in the model.

In the remainder of this paper, we use the modelled velocity profiles

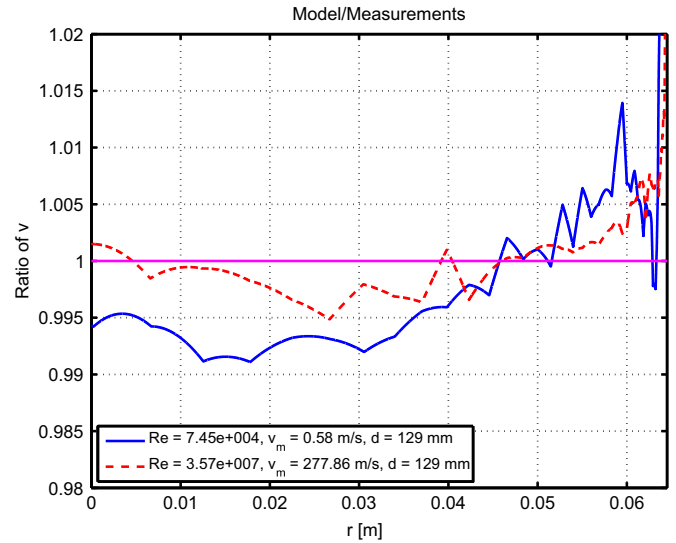


Fig. 2. Ratio of mean velocity profiles.

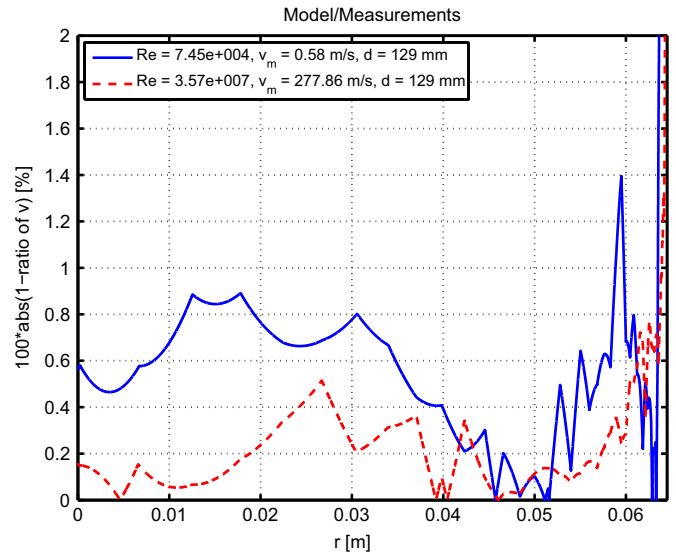


Fig. 3. Shape error of mean velocity profiles.

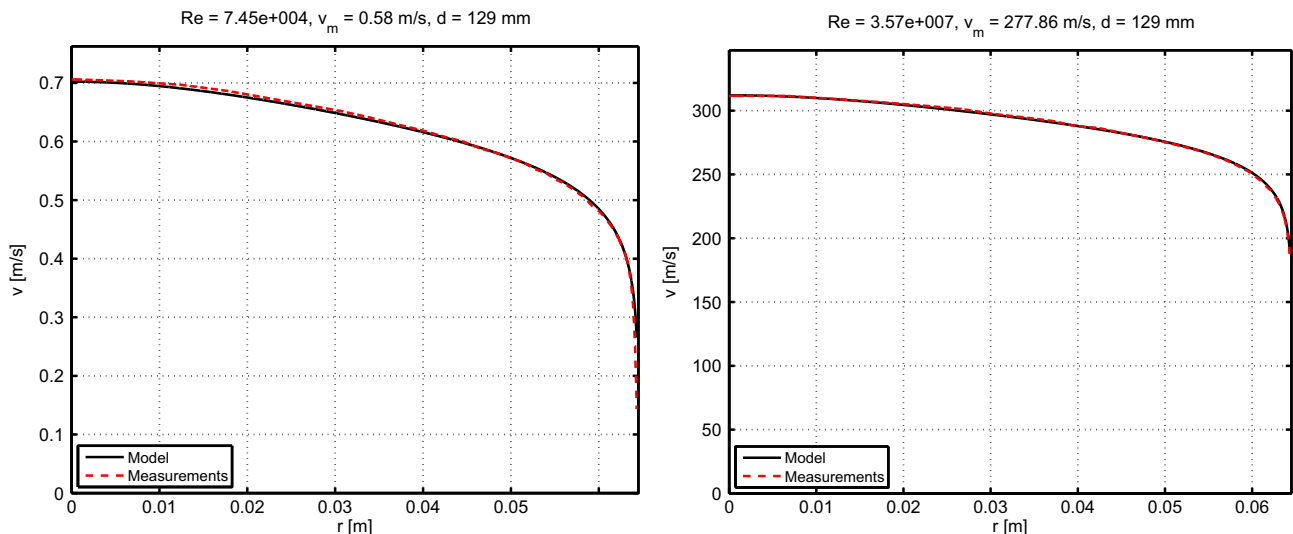


Fig. 1. Mean velocity profiles. Left: $v_m=0.58$ m/s, right: $v_m=277.86$ m/s.

Table 1
Shape error for modelling.

Re	$E_{s,Model/Measurement}$ (smooth wall) (%)	$E_{s,Model/Measurement}$ (rough wall) (%)
0.75×10^5	0.75	0.74
1.44×10^5	0.53	0.52
7.54×10^5	0.18	0.16
13.5×10^5	0.13	0.12
61.1×10^5	0.25	0.17
103×10^5	0.23	0.12
357×10^5	0.22	0.29

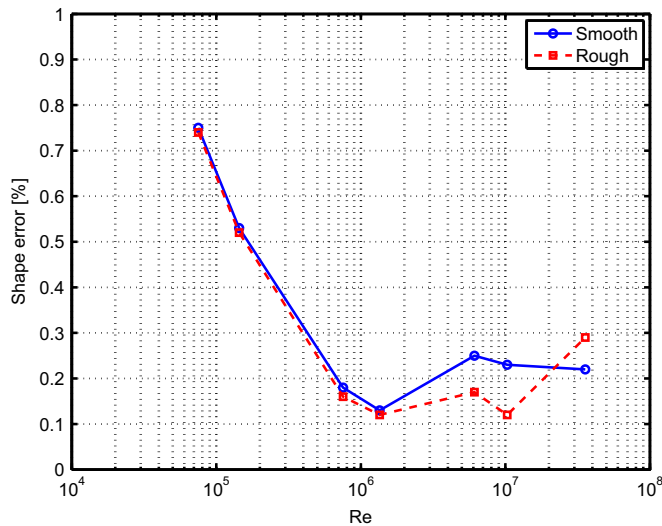


Fig. 4. Shape error of models for smooth and rough walls.

for smooth walls.

4. Computational fluid dynamics simulations

4.1. Software

The computational fluid dynamics (CFD) simulations were done with ANSYS CFX Release 15.0 [13].

The main governing equations are the (Reynolds-averaged) Navier–Stokes equations, the energy equation and the equations of state. The theory is outside the scope of this paper and can be found in [6]. A description of the implementation in ANSYS CFX is provided in [14].

We use the shear-stress transport (SST) turbulence model developed by Menter [15,16].

For simulations of compressible flow, the inlet TI level is set to the recommended default “Medium”, which is 5% [17].

4.2. Working fluid

4.2.1. Incompressible fluid: water

Incompressible CFD simulations are performed with water. The density and temperature of water are set as:

$$\rho = 998.2 \text{ kg/m}^3 \text{ for } T = 293.15 \text{ K} \quad (6)$$

Since the density of water can be assumed to be constant, a value of one atm is taken as the reference pressure and maintained fixed for the whole set of incompressible simulations.

4.2.2. Compressible fluid: air

Air is used for the compressible CFD simulations. In this case, compressed air has to be used to reach high Re .

Physically speaking, the ideal gas law should not be used at high pressure since the assumption of an absence of interparticle interactions no longer holds. Therefore, the ideal gas law

$$\rho = \frac{p_a}{RT_a} \quad (7)$$

should be replaced by the real gas law

$$\rho = \frac{p_a}{ZRT_a} \quad (8)$$

In Eqs. (7) and (8), p_a and T_a are the absolute pressure and temperature, R is the ideal gas constant for air, and Z is the compressibility factor.

Eq. (8) is one of many real gas models; the real gas model we use is from [7] and provided in Appendix A. A comparison between ideal and real air is shown in Appendix B. The conclusion is that, for pressure up to 160 atm, the two models are quite similar.

4.3. Reynolds number

For the incompressible case, the wide range of Re is achieved by changing the mean velocity at the pipe inlet since the viscosity is considered to be constant:

$$Re = \frac{d \times v_m}{\nu}, \quad (9)$$

where d is the pipe diameter and ν is the kinematic viscosity. Eq. (9) is applicable in cases where water is the working fluid since ν is a constant and equal to $1.004 \times 10^{-6} \text{ m}^2/\text{s}$.

The incompressible CFD settings are shown in Table 2. The Mach number stays below 0.2.

For the compressible case, the values of pressure, temperature, and velocity are changed for each simulation in a way to achieve the desired Re . Thus, when air is considered, it is better to write Re in the following manner:

$$Re = \frac{d \times v_m \times \rho}{\mu}, \quad (10)$$

where μ is the dynamic viscosity, $\nu = \frac{\mu}{\rho}$.

In Table 3, the values of density, dynamic viscosity, pressure, and temperature are in agreement with the real gas model described in Appendix A. The Mach number stays below 0.1.

4.4. Geometry and mesh setup

4.4.1. Incompressible flow

ANSYS CFX allows the use of periodic boundary conditions when the fluid has constant properties. This is the case when water is used as the working fluid. More precisely, translational periodic boundary conditions are used. This choice means the pipe can be much shorter and, as a direct consequence, the simulation time much shorter.

The diameter of the pipe is set to $d=0.129 \text{ m}$, which is the same as for the Superpipe. The pipe length is set to three times the pipe

Table 2
Water mean flow velocity according to Re . Temperature 293.15 K, pressure one atm.

Re	Mean flow velocity (m/s)
0.74345×10^5	0.58
1.4458×10^5	1.12
7.5359×10^5	5.89
13.462×10^5	10.50
61.127×10^5	47.55
103.1×10^5	80.20
357.24×10^5	277.86

Table 3
Air properties according to Re .

Re	v_m (m/s)	ρ (kg/m ³)	μ (kg/m s)	p_a (atm)	T_a (K)
2.151×10^5	17.0	1.8	1.8235×10^{-5}	1.5	296
5.369×10^5	22.1	3.4	1.8186×10^{-5}	2.8	294.7
23.63×10^5	19.6	17.2	1.8388×10^{-5}	14.3	295.5
74.90×10^5	19.0	58.0	1.8993×10^{-5}	48	295.2
126.4×10^5	20.0	96.8	1.9754×10^{-5}	80	295.2
183.0×10^5	15.5	208.3	2.2856×10^{-5}	177.2	294.8
278.7×10^5	24.0	204.8	2.2755×10^{-5}	174	295.2
357.2×10^5	30.8	205.4	2.2874×10^{-5}	176.6	297.3

diameter: $L = 3d$.

Meshing is done by matching a structured mesh close to the wall (using the inflation option in ANSYS Meshing) with an unstructured mesh in the pipe center.

The maximum element size in the pipe is one mm.

Since periodic boundary conditions are used, the inlet mean velocity (v_m) has to be imposed indirectly by defining the mass flow:

$$\dot{m} = \rho v_m \left[\frac{\pi d^2}{4} \right] \quad (11)$$

The mesh inflation parameters (first layer height, growth rate, and number of layers) are set according to [17].

Geometry and mesh for the incompressible case (water) are shown in Fig. 5.

More information regarding mesh and simulation setup can be found in Appendix C.

4.4.2. Compressible flow

Periodic boundary conditions cannot be used for the compressible case since the density is not constant along the pipe. The only other option is to make the pipe sufficiently long.

The length of the pipe is chosen such that a fully developed velocity profile is guaranteed. The maximum Re is reached with a mean velocity of 30.8 m/s. See Table 3.

A suitable length of the pipe has to be chosen to have a fully developed velocity profile. The critical length is determined for the highest Re . In Fig. 6, we show the velocity profiles every $10d$ from the

inlet for two cases: the lowest and highest Re . The inlet velocity profile is given by SEM.

To gauge when the profile is approximately constant, we again use the shape error. See Section 3. However, in this case, it is more appropriate to refer to it as a shape change rather than a shape error. In Fig. 7, the downstream and upstream velocity profiles from Fig. 6 are divided to form the ratio:

$$r_{v, \text{Downstream/Upstream}}(r) = \frac{v_{\text{Downstream simulation}}(r)}{v_{\text{Upstream simulation}}(r)} \quad (12)$$

For the low Re case, a pipe length of $70d$ is sufficient to have a fully developed velocity profile since the average shape change of the velocity profile, shown for every $10d$, becomes small for longer pipe lengths. A pipe length of $90d$ is needed for the high Re case. Thus, a pipe length of $100d$ is sufficient for all Re considered.

As for the incompressible case, meshing is done by matching a structured mesh close to the wall with an unstructured mesh in the pipe center.

The maximum element size in the pipe is 4.5 mm, which is 4.5 times larger than for the incompressible case. This is because we need a long pipe for the compressible case; a one mm maximum element size would be too demanding in terms of computational cost.

Geometry and mesh for the compressible case (air) are shown in Fig. 8.

5. Mean velocity profile

5.1. Incompressible flow

In this section, the incompressible flow (water) mean velocity profiles are analysed.

In Fig. 9, the measured, modelled, and simulated mean velocity profiles are shown as a function of the pipe radius. The modelled velocity profile is in close agreement with the measurement. The simulated model underestimates the core velocity and overestimates the velocity closer toward the pipe wall.

In Fig. 10, the shape errors for the velocity profiles in Fig. 9 are displayed. The shape error for the modelled profile is 0.22% and the shape error for the simulation is 1.32%.

Table 4 summarizes all the simulations, with their respective shape errors. The shape error measures the difference, in terms of mean

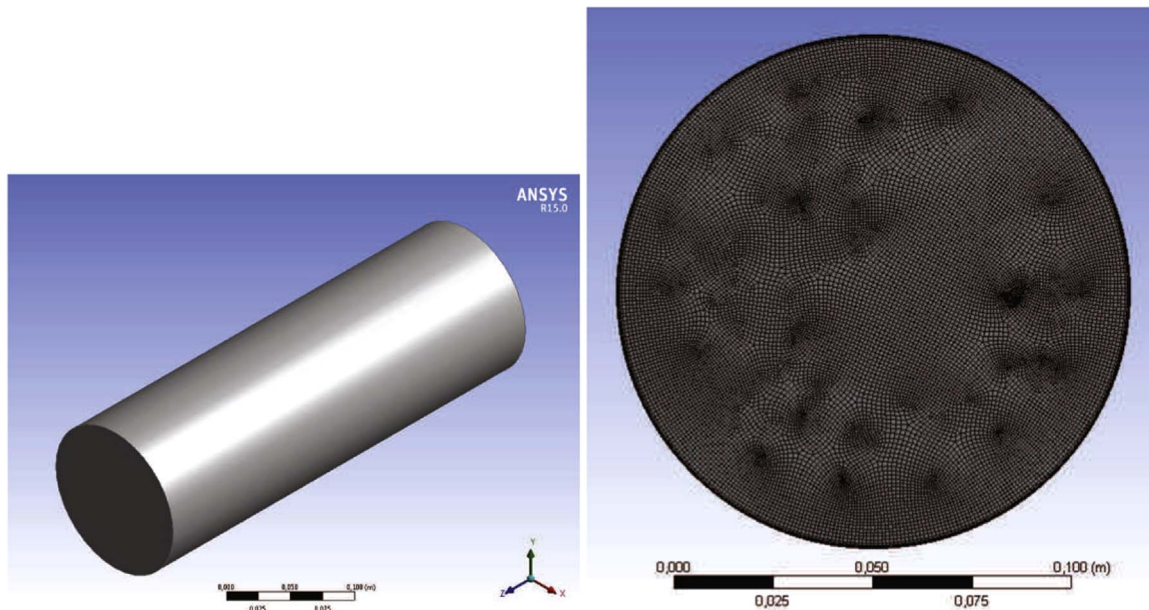


Fig. 5. Incompressible flow. Left: geometry; right: mesh.

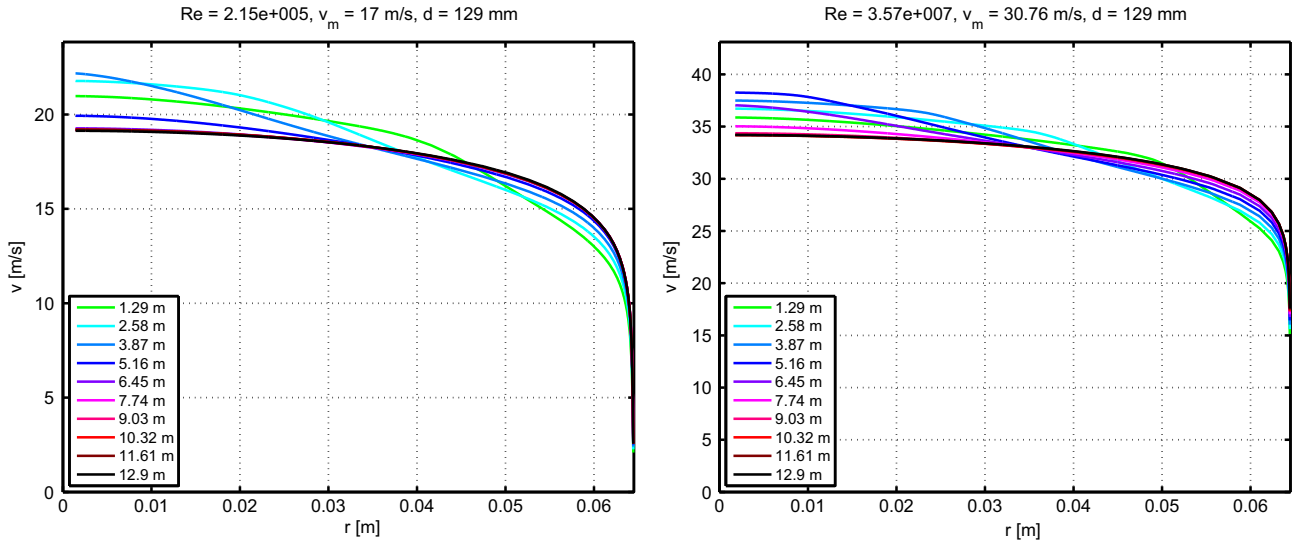


Fig. 6. Velocity profile shape every 10d from inlet, left: $Re = 2.15 \times 10^5$, right: $Re = 3.57 \times 10^7$.

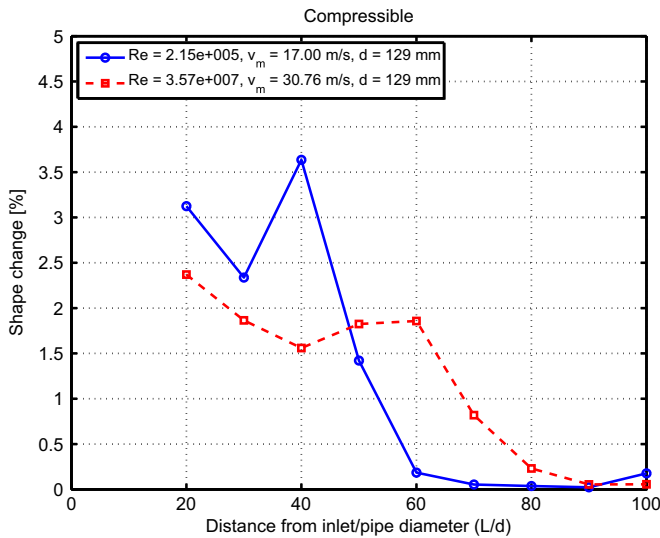


Fig. 7. Velocity profile shape change every 10d from inlet.

velocity profile shape, between the simulated or modelled profile and the measured profile.

5.2. Compressible flow

Compressible simulations are done by using real air as the fluid.

The shape error for compressible simulations does not have a minimum at the outlet. See Fig. 11. The distance from the inlet to where the closest alignment with measurements is achieved is shown in Table 5 for all cases.

As for the incompressible simulations, we illustrate the results for $Re = 3.57 \times 10^7$. Very good agreement of the simulations with measurements is observed for this case. See the mean velocity profiles in Fig. 12: measured, modelled, and simulated profiles are almost identical.

The good quality of the compressible simulations is confirmed by the shape error. See Fig. 13. The shape error for the best simulation is plotted. The simulation shape error is 0.26%, which is almost as small as the modelled shape error (0.22%).

In Table 5, the shape errors between simulations and measurements are summarized. The agreement is significantly improved compared to the incompressible case. This means that the real gas

model and the geometry setup (long pipe) used for the compressible case produce higher quality simulations.

The shape errors for incompressible (Table 4) and compressible (Table 5) simulations are combined in Fig. 14.

The incompressible error is largest and decreases with increasing Re . This behaviour is also seen for the modelling results in Fig. 4.

The compressibility error is lower and does not vary strongly with Re .

6. Turbulence intensity

6.1. Definition and background

The turbulence intensity (TI) I is defined as:

$$I = \frac{v_{RMS}}{v} \quad (13)$$

where v_{RMS} is the RMS of the turbulent velocity fluctuations. This can be expressed using the different components:

$$v_{RMS} = \sqrt{\frac{1}{3}[(v_{RMS,x})^2 + (v_{RMS,y})^2 + (v_{RMS,z})^2]} \quad (14)$$

where

$$k = \frac{1}{2}[(v_{RMS,x})^2 + (v_{RMS,y})^2 + (v_{RMS,z})^2] \quad (15)$$

is the turbulent kinetic energy (TKE) (per unit mass).

Combining Eqs. (14) and (15), we write the relationship between velocity and kinetic energy of the fluctuations:

$$v_{RMS} = \sqrt{\frac{2}{3}k} \quad (16)$$

The TKE can be extracted directly from CFX. Examples for low and high Re are shown in Fig. 15. The TKE has a maximum close to the pipe wall.

The mean TKE versus distance from the pipe inlet is shown in Fig. 16. In general, the TKE is higher for larger Re . The maximum TKE is close to the position where the simulated mean flow velocity is most closely aligned with the measurements. See Table 5.

The TI can either be defined on the pipe axis (as in Eq. (1)):

$$I_{pipe\ axis} = \frac{v_{RMS, pipe\ axis}}{v_{pipe\ axis}} \quad (17)$$

or over the pipe area:

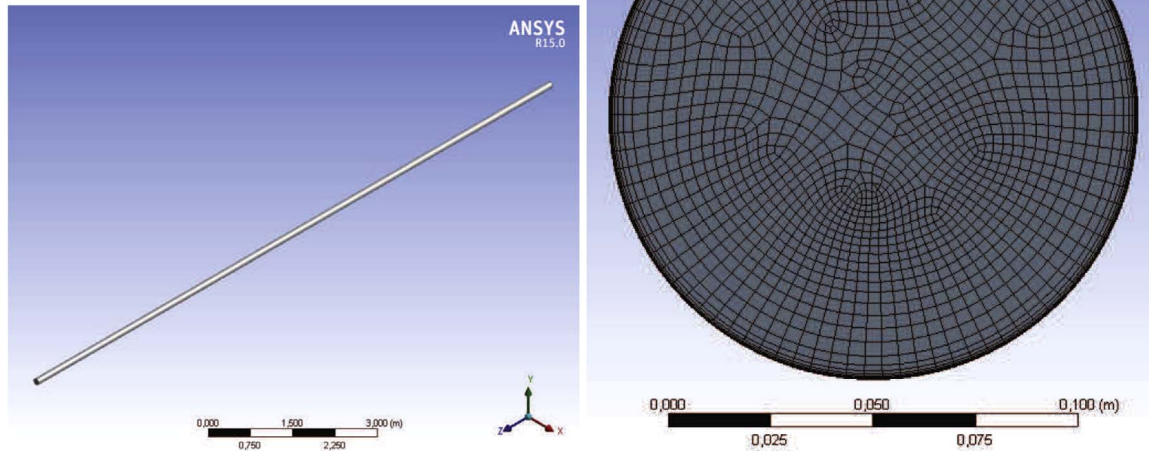


Fig. 8. Compressible flow. Left: geometry; right: mesh.

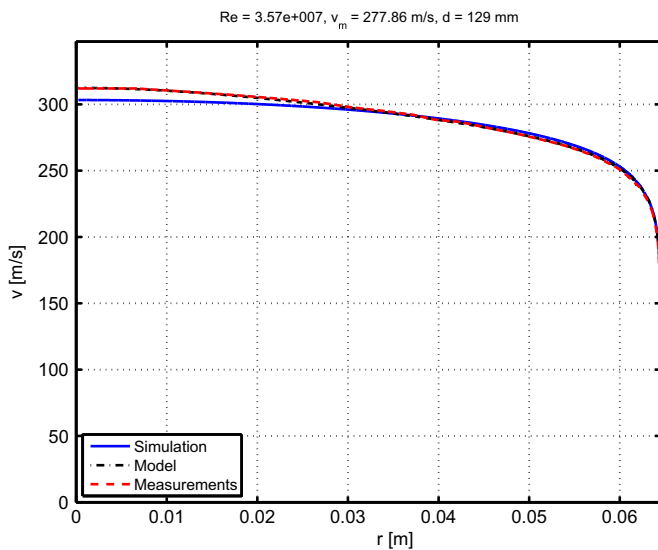


Fig. 9. Mean velocity profiles for incompressible flow.

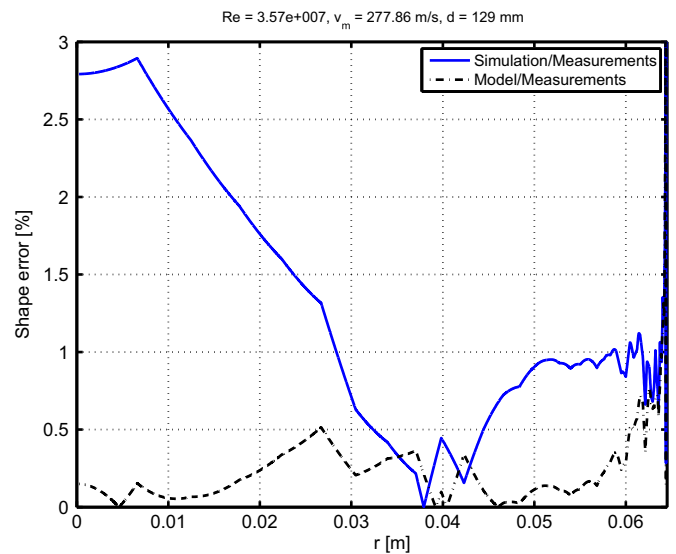


Fig. 10. Shape error of mean velocity profiles for incompressible flow.

$$I_{\text{pipe area}} = \frac{1}{N} \times \sum_r \frac{v_{\text{RMS}}(r)}{v(r)} \tag{18}$$

Note that the TI at the wall diverges due to the no-slip boundary condition. In the following, we calculate TI over the pipe area as close to the wall as we have simulations or measurements.

In the following sections, the scaling of Eq. (1) is compared with the scaling obtained from the CFD simulations and from measurements. The simulated and measured data is fitted to a power-law expression:

$$I_{\text{Fit}} = a \times Re^b, \tag{19}$$

where a and b are fit parameters.

Note that a is used for the pipe radius in Section 3.

6.2. Incompressible flow

The seven incompressible simulations, summarized in Table 2, are represented as seven data points in the TI versus Re plots below.

To be able to extract the TI value on the axis of the pipe (to be

Table 4
Shape error for incompressible simulations.

Re	$E_{s, \text{Simulation}} (\%)$
0.74×10^5	3.02
1.45×10^5	2.55
7.54×10^5	1.84
13.5×10^5	1.68
61.1×10^5	1.65
103×10^5	1.57
357×10^5	1.35

precise, the TKE is extracted and the TI is calculated afterward), a point is defined on the pipe axis.

For the TI on the axis of a straight pipe, we found the following expression:

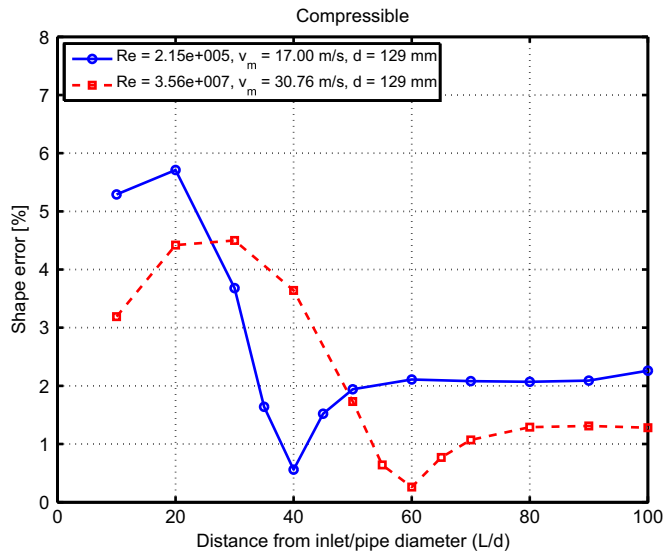


Fig. 11. Compressible flow, shape error every 10d from inlet.

Table 5
Shape error for compressible simulations.

Re	L/d	$E_{s,Simulation}$ (%)
2.15×10^5	40	0.56
5.37×10^5	45	0.37
23.6×10^5	55	0.38
74.9×10^5	55	0.49
126×10^5	55	0.19
183×10^5	60	0.27
278×10^5	60	0.41
357×10^5	60	0.26

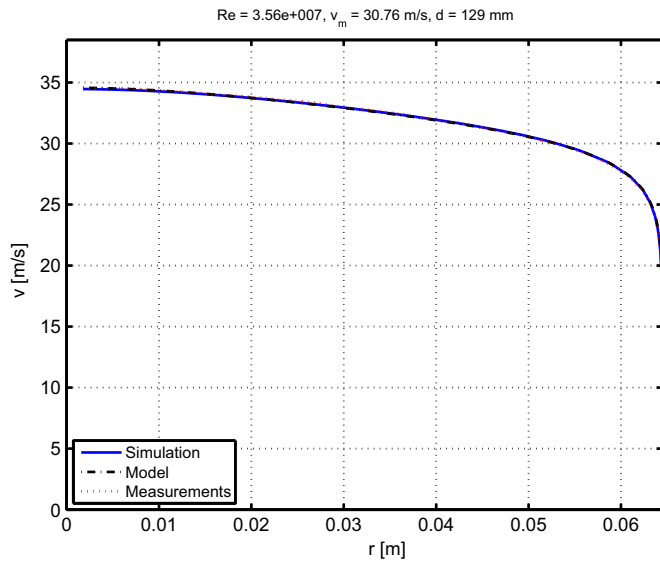


Fig. 12. Mean velocity profiles for compressible flow.

$$I_{Incompressible\ CFD, pipe\ axis} = 0.0853 \times Re^{-0.0727} \quad (20)$$

The CFD points and resulting fit are compared to Eq. (1) in Fig. 17. Our CFD-based scaling of TI leads to a slower decrease of TI with increasing Re compared to Eq. (1). But overall, the TI range is comparable.

For applications, it is more interesting to know the TI in an average

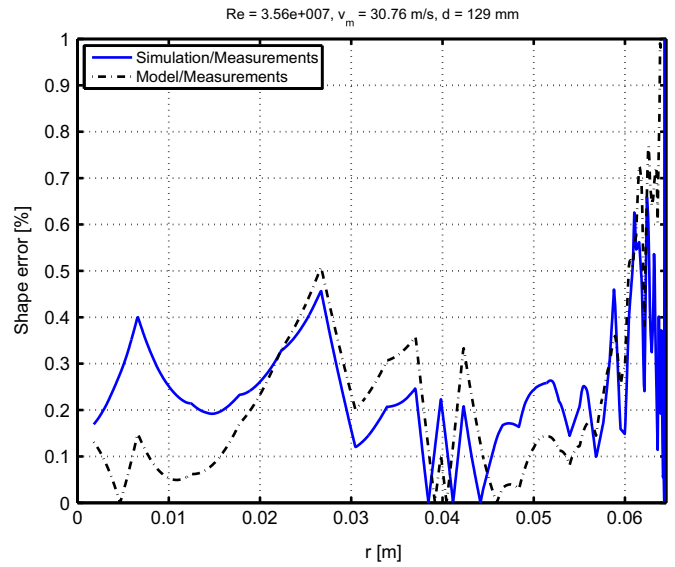


Fig. 13. Shape error of mean velocity profiles for compressible flow.

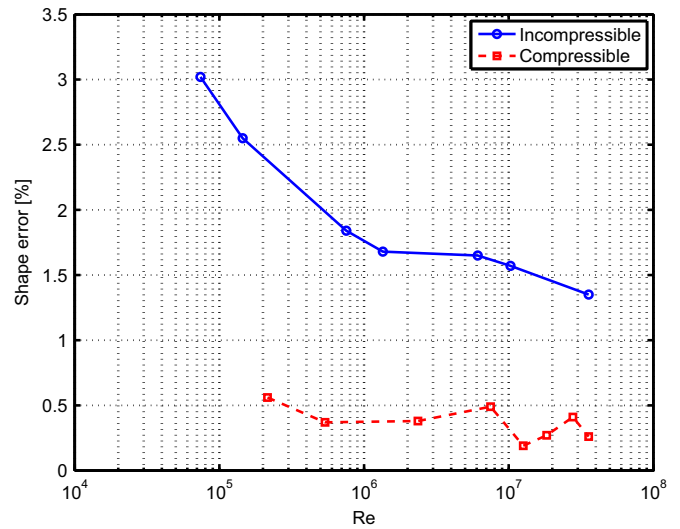


Fig. 14. Shape error of incompressible and compressible simulations.

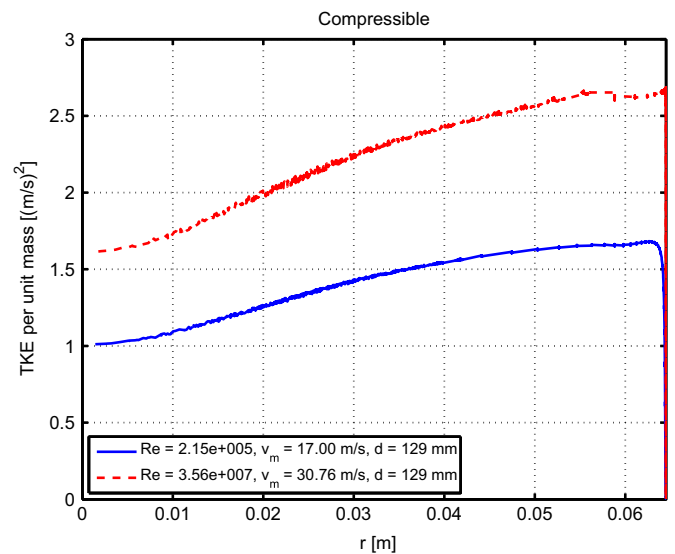


Fig. 15. Turbulent kinetic energy for compressible flow.

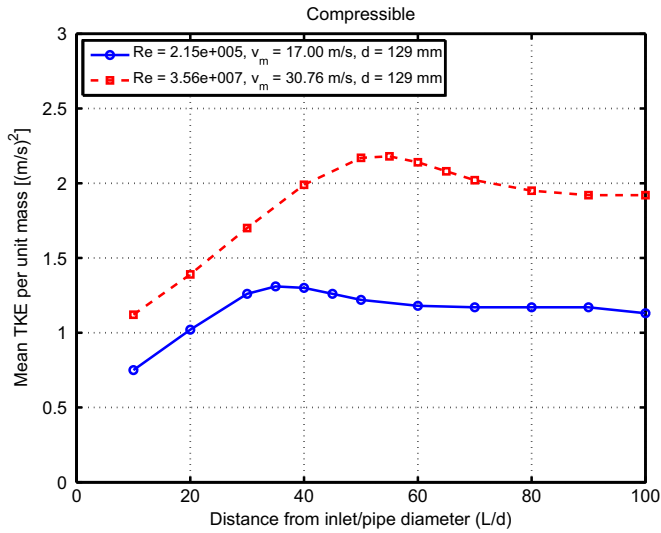


Fig. 16. Compressible flow, mean TKE every 10d from inlet.

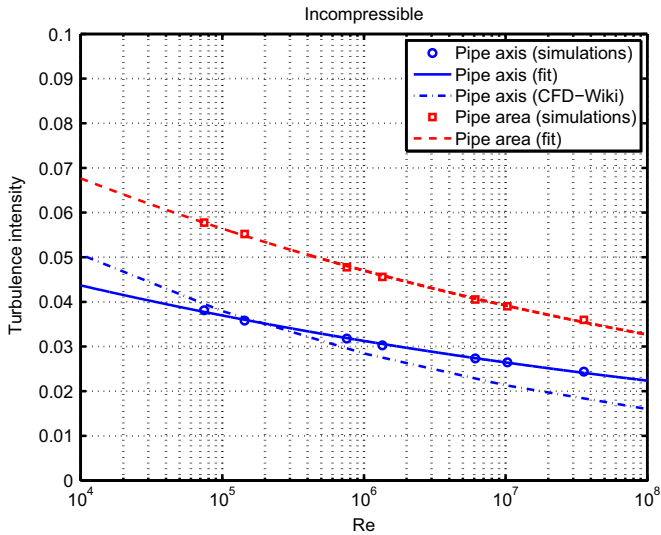


Fig. 17. Turbulence intensity for incompressible flow.

sense, i.e. averaged over the pipe area instead of only on the pipe axis. The scaling for the TI averaged over the pipe cross-sectional area is:

$$I_{\text{Incompressible CFD, pipe area}} = 0.140 \times Re^{-0.0790} \quad (21)$$

The CFD simulation points and fit are shown in Fig. 17. In general, the TI level is higher. This is because the maximum TI is not located on the pipe axis but close to the wall. See Fig. 18.

6.3. Compressible flow

The eight compressible simulations are summarized in Table 3.

For the TI on the axis of the pipe, we obtained the following formula:

$$I_{\text{Compressible CFD, pipe axis}} = 0.0947 \times Re^{-0.0706} \quad (22)$$

In Fig. 19, we compare Eq. (22) to Eq. (1). The CFD-based TI is larger than the one from Eq. (1) for the Re simulated. Note also that the scatter of the simulations is larger than for the incompressible case. This is most likely because the mean velocity profile changes fast with L/d . See Fig. 11. We calculate the error in steps of $5 L/d$, and this may be the cause of the scatter.

For the TI averaged over the entire cross-sectional area, we find the

following scaling power law:

$$I_{\text{Compressible CFD, pipe area}} = 0.153 \times Re^{-0.0779} \quad (23)$$

This scaling is presented in Fig. 19.

6.4. Comparison between incompressible and compressible flow

In Fig. 20, the CFD results obtained are compared for incompressible and compressible flow. A somewhat larger TI is seen for compressible flow.

The fit parameters for the incompressible and compressible simulations are collected in Table 6.

6.5. Compressible flow: comparison of simulations to measurements

Combined measurements of the mean velocity profile and the streamwise Reynolds stress profile are published in [18,19]. These Hultmark measurements have recently been made publicly available [20]. We have combined the measurements to yield a measured TI, see Fig. 21. Note that strictly speaking this is the streamwise TI as opposed to the total TI from the simulations. Keeping this in mind, we will compare the simulated and the measured TI below. The general trend of an increasing TI towards the wall is shown in Fig. 18 for an incompressible simulation is also observed in the compressible measurements in Fig. 21.

Using r_n as the normalized pipe radius (0–1), the measured TI profiles in Fig. 21 can be fitted to:

$$I_{\text{Compressible measurements, total}}(r_n) = I_{\text{Core}}(r_n) + I_{\text{Wall}}(r_n) = [\alpha + \beta \times r_n^\gamma] + [\delta \times \ln(1 - r_n)]^\epsilon, \quad (24)$$

where $\alpha, \beta, \gamma, \delta$ and ϵ are fit parameters. The core TI shape is inspired by what is observed for electron density fluctuations in magnetically confined fusion plasmas [21]. More details on fits to measured TI profiles can be found in Appendix D.

For the TI on the axis of the pipe (see Fig. 22), we obtained the following formula:

$$I_{\text{Compressible measurements, pipe axis}} = 0.0550 \times Re^{-0.0407} \quad (25)$$

For the TI averaged over the entire cross-sectional area (see Fig. 22), we find the following scaling power law:

$$I_{\text{Compressible measurements, pipe area}} = 0.227 \times Re^{-0.100} \quad (26)$$

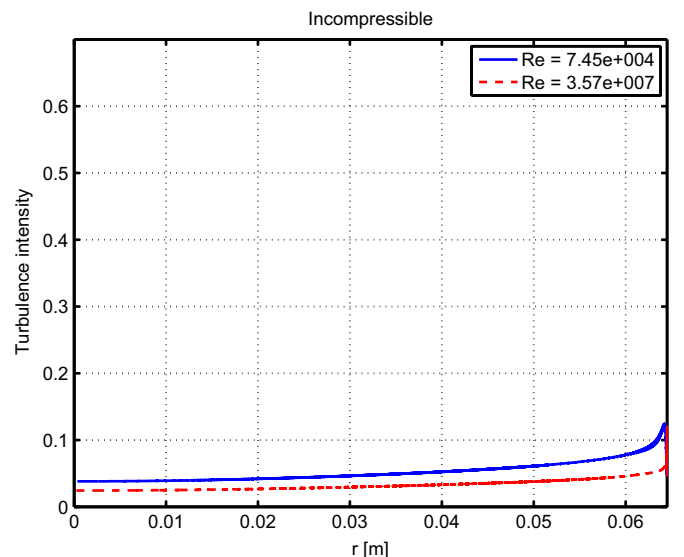


Fig. 18. Turbulence intensity for incompressible flow.

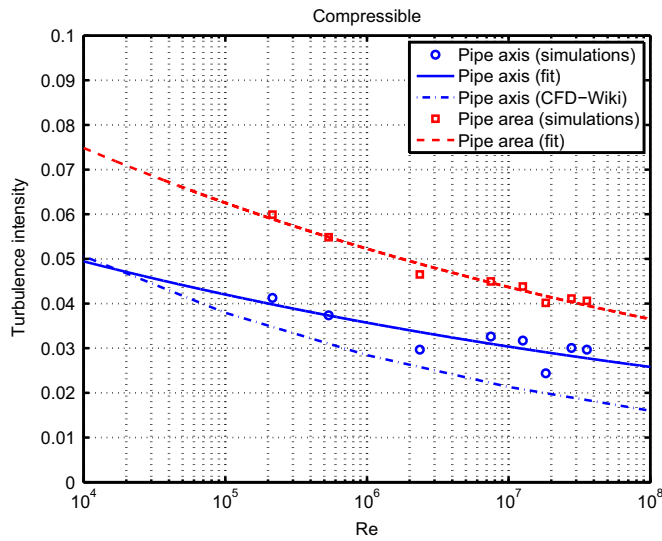


Fig. 19. Turbulence intensity for compressible flow.

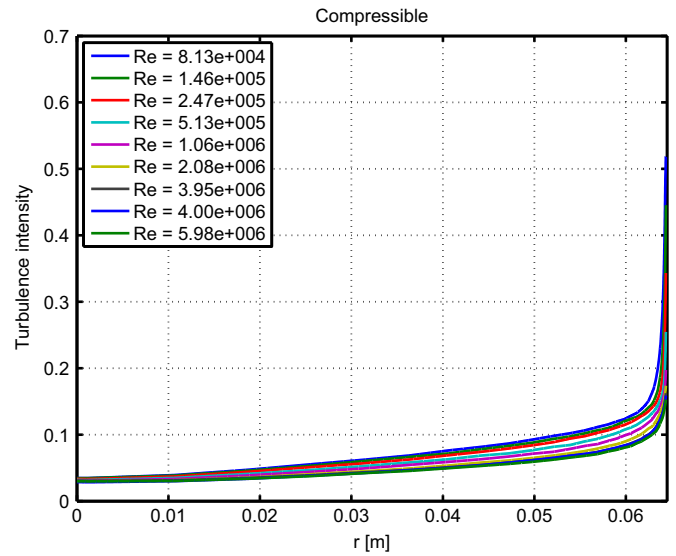


Fig. 21. Measured turbulence intensity for compressible flow.

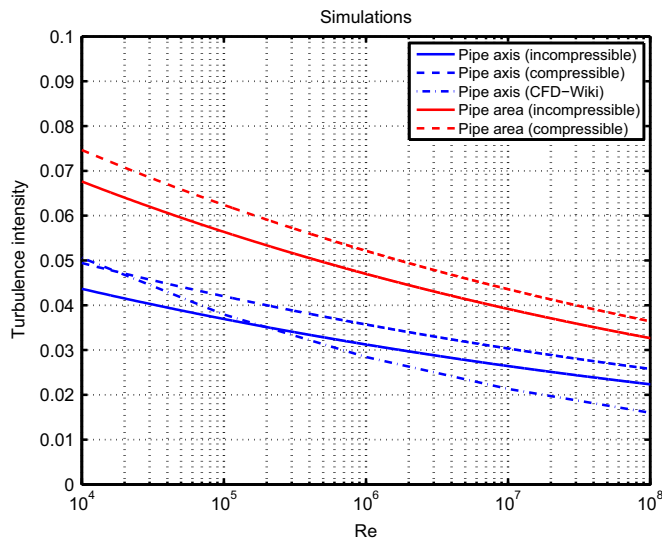


Fig. 20. Turbulence intensity for incompressible and compressible flow.

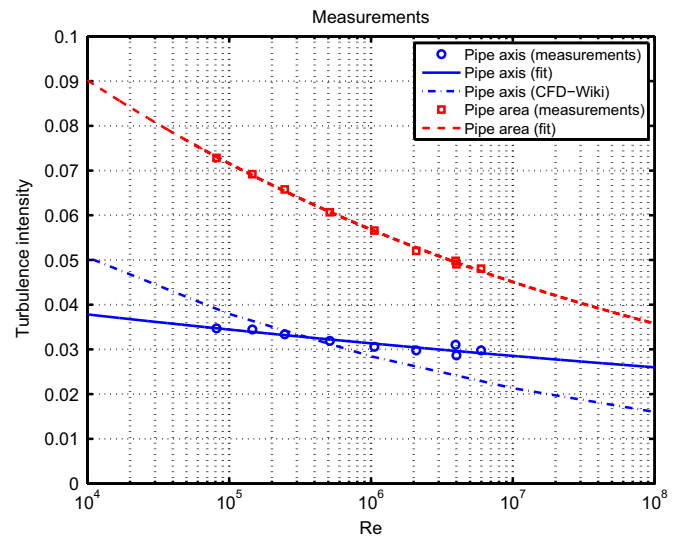


Fig. 22. Turbulence intensity for measured compressible flow.

Table 6
TI fit parameters for simulations.

Case	<i>a</i>	<i>b</i>
Incompressible simulations, pipe axis	0.0853	-0.0727
Incompressible simulations, pipe area	0.140	-0.0790
Compressible simulations, pipe axis	0.0947	-0.0706
Compressible simulations, pipe area	0.153	-0.0779

The TI fit parameters for measured and simulated compressible flow are combined in Table 7.

The deviation of the simulation-based from the measurement-based TI fit parameters is available in Table 8. An increase (decrease) of one fit parameter is countered by a decrease (increase) of the other fit parameter, respectively. This implies that the TI from the simulations and the measurements is close for the *Re* considered – but the scaling with *Re* is different. The deviation of the fit parameters is largest for the pipe axis fits.

Table 7
TI fit parameters for compressible measurements and simulations.

Case	<i>a</i>	<i>b</i>
Compressible measurements, pipe axis	0.0550	-0.0407
Compressible measurements, pipe area	0.227	-0.100
Compressible simulations, pipe axis	0.0947	-0.0706
Compressible simulations, pipe area	0.153	-0.0779

Table 8
Percentage deviation of simulation-based from measurement-based TI fit parameters.

Case	<i>a</i> deviation (%)	<i>b</i> deviation (%)
Compressible simulations, pipe axis	72	-73
Compressible simulations, pipe area	-33	22

7. Application example: compressible flow

It is instructive to relate the fluctuating and mean velocities for some cases that resemble what can be found for flowmeters.

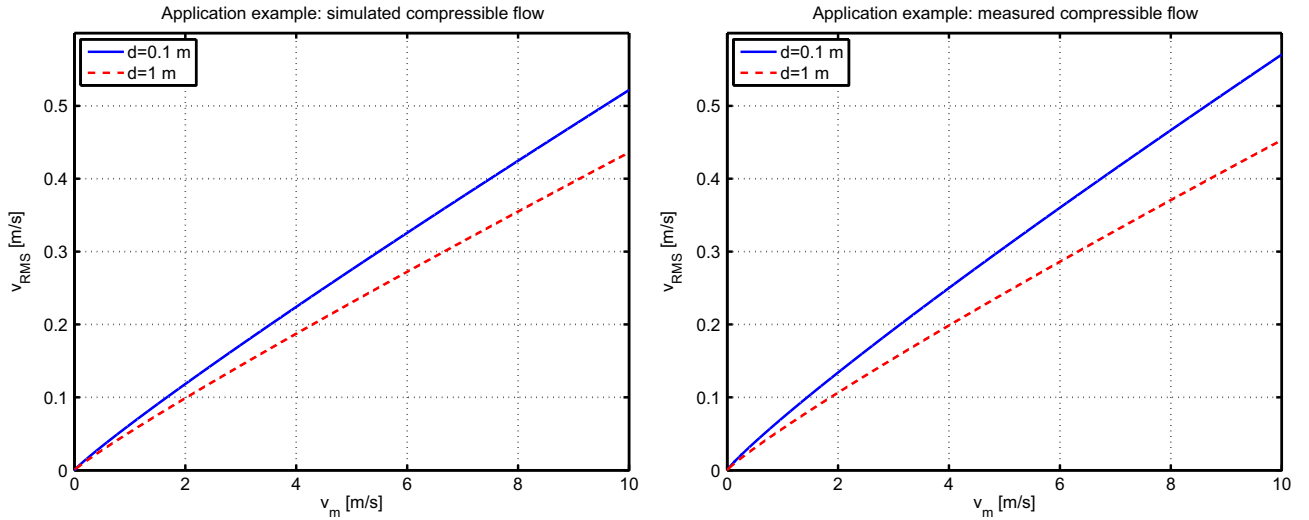


Fig. 23. Relationship between mean and fluctuating velocity for compressible flow. Left: simulated, right: measured.

Here, we consider two pipes with pipe radii of 0.1 and 1 m, respectively.

Using Eq. (19), we can express the fluctuating velocity as a function of the mean velocity:

$$v_{\text{RMS}} = a \times \left(\frac{d \times \rho}{\mu} \right)^b \times v_m^{1+b} \quad (27)$$

We use a and b from Eqs. (23) and (26) for Fig. 23 (pipe area fits). We use the density and dynamic viscosity for water at room temperature.

For these mean flow velocities, the simulation-based scaling is quite close to the measurement-based scaling. Note that the pipe diameter does not alter the scaling significantly.

8. Conclusions

In this paper, we compared measured, modelled, and simulated mean velocity profiles.

Once the quality of the simulations was deemed sufficient, we used the simulated turbulent kinetic energy to make scaling formulae for turbulence intensity as a function of the Reynolds number.

This was done for both incompressible and compressible smooth pipe flow. Mach numbers were below 0.2 and 0.1, respectively. The incompressible simulations were done with periodic boundary conditions, and compressible simulations were done using a long pipe.

Agreement between measurements and simulations of the mean velocity profile was best when a real gas model was used. Two main reasons for this have been identified: (i) the real gas model is more exact and (ii) the quality of the periodic (incompressible) simulation is not as high as the long pipe (compressible) simulation. The relative

Appendix A. Real gas

The model of real gas [7], which has been implemented in ANSYS, is described below.

Eq. (A.1) is the modified version of the ideal gas law using the compressibility factor Z . p_a and T_a are the absolute pressure and temperature, ρ is the density, and $R = 287 \text{ J/kg K}$ is the universal gas constant specified for air.

$$\rho = \frac{p_a}{ZRT_a} \quad (A.1)$$

The compressibility factor Z is evaluated from the following equation:

$$Z(p_a, T_a) = 1 + Z_1(p_a - 1) + Z_2(p_a - 1)^2 + Z_3(p_a - 1)^3 \quad (A.2)$$

importance of these contributions is a topic for future investigation.

Based on simulations, the turbulence intensity scaling with the Reynolds number was found on the pipe axis and also averaged over the pipe area. The resulting expressions were similar for incompressible and compressible flow.

The simulated turbulence scaling for compressible flow was compared to scaling derived from measurements. The differences seem to be caused mainly by a discrepancy between the simulated and measured turbulent velocity fluctuations.

As far as we know, this paper is the first to document the scaling behaviour of I with Re found using both measurements and simulations. We recommend that these expressions are used instead of Eq. (1).

Our future research in straight pipe turbulence will focus on additional compressible simulations to study turbulence scaling:

- For rough pipes.
- For other turbulence intensity levels at the inlet (e.g. one and ten %).
- For high-speed (above Mach 0.5) compressible flow:
 1. It is an open question for how high Mach numbers the scaling remains accurate. From aerodynamics, compressibility effects become significant above Mach 0.3. We expect the scaling to be valid at least up to Mach 0.2. However, we need to identify suitable measurements to extend our work in this direction.

Acknowledgement

We thank Professor A.J. Smits for making the Superpipe data publicly available [11,20].

Table A1

Compressibility factor coefficients for real air. The atm superscripts refer to the three rows: Top row is atm⁻¹ and bottom row is atm⁻³.

Coefficient	A (atm ^{-1/2/-3})	B (K ⁻¹ atm ^{-1/2/3})	C (K ⁻² atm ^{-1/2/3})	D (K ⁻³ atm ^{-1/2/3})
Z ₁	-9.5378 × 10 ⁻³	5.1986 × 10 ⁻⁵	-7.0621 × 10 ⁻⁸	0
Z ₂	3.1753 × 10 ⁻⁵	-1.7155 × 10 ⁻⁷	2.4630 × 10 ⁻¹⁰	0
Z ₂	6.3764 × 10 ⁻⁷	-6.4678 × 10 ⁻⁹	2.1880 × 10 ⁻¹¹	-2.4691 × 10 ⁻¹⁴

The coefficients Z₁, Z₂, and Z₃ depend on the absolute temperature as shown below:

$$Z_1 = A_1 + B_1 T_a + C_1 T_a^2 + D_1 T_a^3 \tag{A.3}$$

$$Z_2 = A_2 + B_2 T_a + C_2 T_a^2 + D_2 T_a^3 \tag{A.4}$$

$$Z_3 = A_3 + B_3 T_a + C_3 T_a^2 + D_3 T_a^3 \tag{A.5}$$

The A, B, C, and D coefficients are summarized in Table A1.

The viscosity has also been implemented as a real gas variable:

$$\mu(T_a, \rho) = \mu_0(T_a) + \mu_1(\rho), \tag{A.6}$$

where μ is the dynamic viscosity, which is split into two terms: μ_0 , which is a function of the absolute temperature, and μ_1 , which depends on the density only.

The first term on the right-hand side of Eq. (A.6) is Sutherland's viscosity for air:

$$\mu_0(T_a) = \frac{1.458 \times 10^{-6} \times T_a^{1.5}}{110.4 + T_a} \tag{A.7}$$

The second right-hand side term of Eq. (A.6) is described as follows:

$$\mu_1(\rho) = E_0 + E_1 \rho + E_2 \rho^2, \tag{A.8}$$

where $E_0 = -5.516 \times 10^{-8}$ kg/m s, $E_1 = 1.1 \times 10^{-8}$ m²/s and $E_2 = 5.565 \times 10^{-11}$ m⁵/kg s.

Appendix B. Ideal vs. real gas

Here, we compare the governing equation for real gas (Eq. (A.1) in Appendix A) to the ideal gas formulation, see Fig. B1. The comparison is made for 293 K and 298 K since this is the range covered by the Superpipe measurements. It can be seen that, up to 160 atm, the density provided by the two models is exactly the same. At pressure higher than 160 atm, the first small differences in density begin to appear.

The relationship between dynamic viscosity and density is shown for real gas in Fig. B2. Again, two temperatures covering the Superpipe range are included. The formula for the dynamic viscosity is Eq. (A.6) in Appendix A.

Summing up, we can conclude that air behaves as an ideal gas up to a pressure of 160 atm. The dynamic viscosity is not constant; it is a function of both temperature and density.

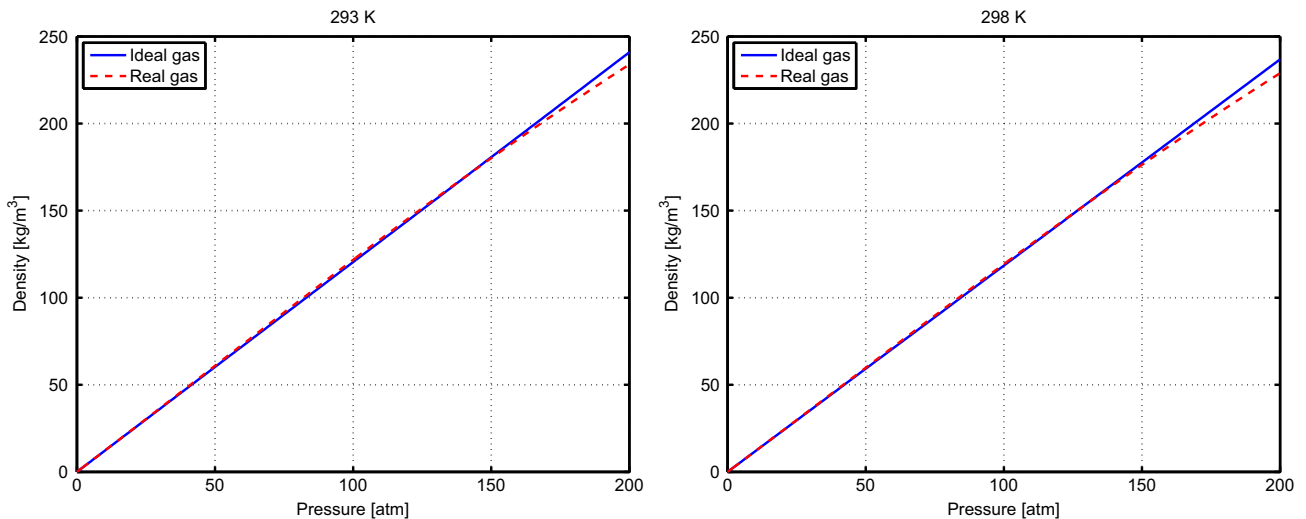


Fig. B1. Density versus pressure, left: 293 K, right: 298 K.

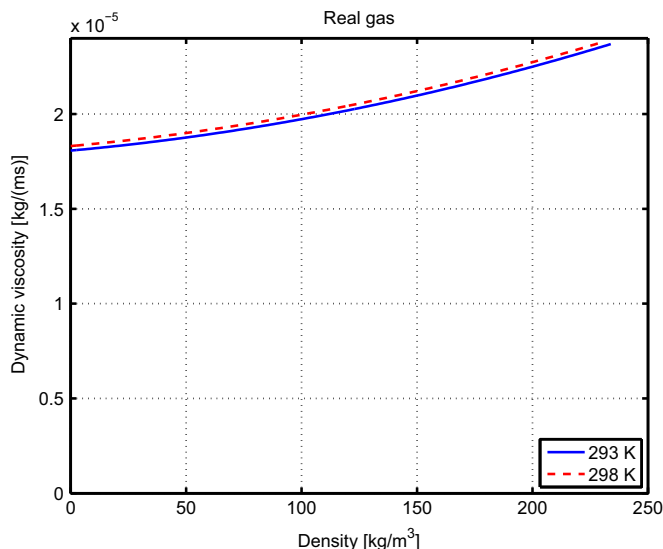


Fig. B2. Dynamic viscosity versus density.

Appendix C. Mesh statistics and simulation setup

C.1. Common settings

Settings used for both incompressible and compressible CFD simulations [17]:

- Cylinder radius 0.0645 m.
- Swept mesh.
- Turbulence model: SST.
- High resolution turbulence numerics.
- Residual target 10^{-4} RMS.
- Conservation target 0.01.

C.1.1. Boundary layer

As stated in Section 4.4, we use a structured mesh close to the wall. The elements are quadrilateral in 2D and hexahedral in 3D. The boundary layer is defined using three parameters, see Tables C1 and C2:

- Height (first layer height): The distance of the first mesh node from the wall
- Growth (growth rate): A factor determining how fast the distance between nodes increases
- Layers: The number of mesh nodes in the boundary layer

C.1.2. Pipe center

The unstructured mesh elements are a mixture of triangular and quadrilateral in 2D. In 3D, this becomes triangular prisms and hexahedrons.

C.2. Incompressible simulations

For incompressible simulations, we use a pipe length of three times the pipe diameter. The maximum mesh size is set to one mm. This leads to a model size of between seven and nine million nodes/elements, see Table C1. The simulation is periodic, with a pressure update multiplier of 0.05, and the domain interface target is 0.01.

Table C1
Incompressible CFD settings.

Re	Height (m)	Growth	Layers	Nodes	Elements	T_{ref} (°C)	p_{ref} (atm)
0.74345×10^5	3×10^{-5}	1.075	48	9 759 596	9 667 430	20	1
1.4458×10^5	1×10^{-5}	1.2	25	7 219 535	7 140 084	20	1
7.5359×10^5	3×10^{-6}	1.3	22	7 933 758	7 850 400	20	1
13.462×10^5	2×10^{-6}	1.35	20	6 632 064	6 551 769	20	1
61.127×10^5	5×10^{-7}	1.5	18	6 813 090	6 731 655	20	1
103.1×10^5	3×10^{-7}	1.55	18	7 187 700	7 107 529	20	1
357.24×10^5	1×10^{-7}	1.65	18	7 325 327	7 242 408	20	1

Table C2

Compressible CFD settings. For some cases, the reference temperature and pressure correspond exactly to Superpipe (SP) measurements.

Re	Height (m)	Growth	Layers	Nodes	Elements	T_{ref} (°C)	p_{ref} (atm)
2.151×10^5	1×10^{-5}	1.2	33	11 575 774	11 442 810	22.85	1.5
5.369×10^5	5×10^{-6}	1.25	30	11 687 548	11 554 545	21.6 (SP)	2.85 (SP)
23.63×10^5	1×10^{-6}	1.4	25	10 432 240	10 299 675	22.3 (SP)	14.33 (SP)
74.90×10^5	4×10^{-7}	1.5	23	9 055 685	8 928 468	22	48
126.4×10^5	2×10^{-7}	1.6	21	7 747 500	7 631 946	22	80
183.0×10^5	2×10^{-7}	1.6	21	7 747 500	7 631 946	21.6(SP)	177.2 (SP)
278.7×10^5	1×10^{-7}	1.65	21	8 476 892	8 354 094	22	174
357.2×10^5	1×10^{-7}	1.65	21	8 476 892	8 354 094	24.1(SP)	176.6 (SP)

Since we use periodic boundary conditions, we set a mass flow rate to get the required Re .

C.3. Compressible simulations

For compressible simulations, we use a pipe length of 100 times the pipe diameter. The maximum mesh size is set to 4.5 mm. This leads to a model size of between eight and 11 million nodes/elements. See Table C2. The inlet velocity is the SEM profile, and the outlet is static pressure (0 Pa relative pressure).

The inlet boundary condition is velocity and the outlet is static pressure.

Appendix D. Fits to measured turbulence intensity profiles

Two examples of fits using Eq. (24) are shown in Fig. D1.

Fits for all measured Re have been performed. The resulting fit parameters are shown versus Re in Fig. D2. Fit parameter α is the TI on the pipe axis, see also Fig. 22.

Typically, the maximum deviation of the fits from the measurements is below 5%, see Fig. D3. For the two cases where there is a larger deviation, this is due to an imperfect fit close to the wall.

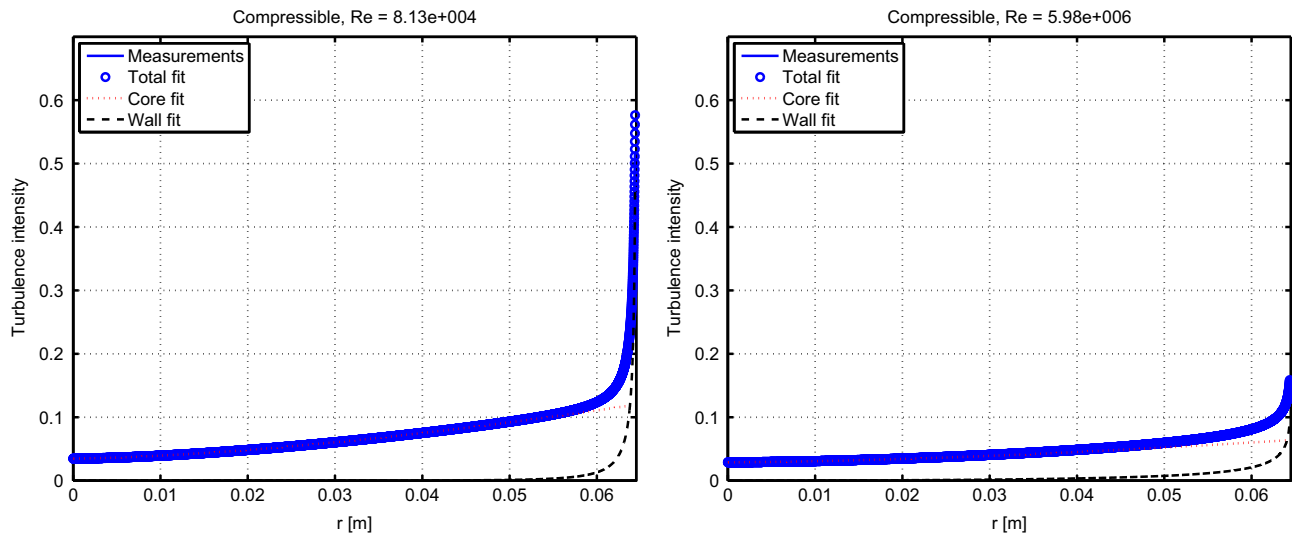


Fig. D1. Measured TI profiles with total, core and wall fits. Left: $Re = 8.13 \times 10^4$, right: $Re = 5.98 \times 10^6$.

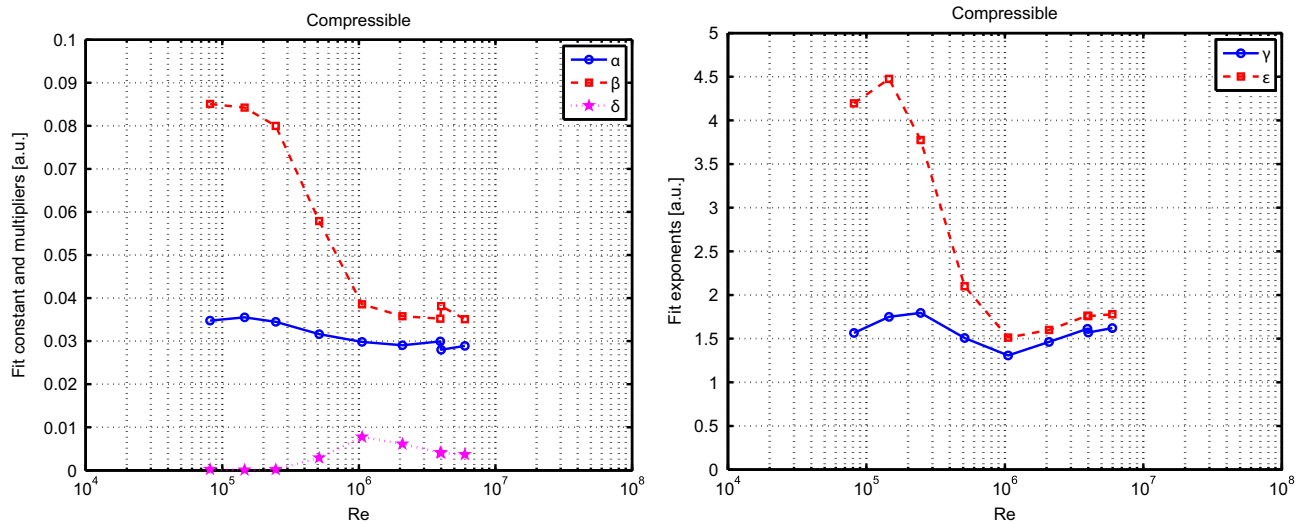


Fig. D2. Fit parameters as a function of Re.

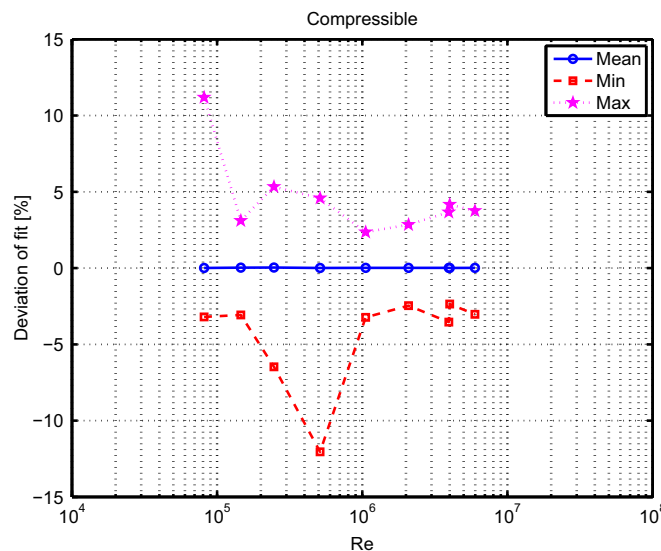


Fig. D3. Deviation of fits to measurements.

References

[1] I. Marusic, B.J. McKeon, P.A. Monkewitz, H.M. Nagib, A.J. Smits, K.R. Sreenivasan, Wall-bounded turbulent flows at high Reynolds numbers: recent advances and key issues, *Phys. Fluids* 22 (2010) 065103.
 [2] A.J. Smits, B.J. McKeon, I. Marusic, High-Reynolds number wall turbulence, *Annu. Rev. Fluid Mech.* 43 (2011) 353–375.
 [3] I. Marusic, J.P. Monty, M. Hultmark, A.J. Smits, On the logarithmic region in wall turbulence, *J. Fluid Mech.* 716 (2013) R3.
 [4] H. Schlichting, K. Gersten, *Boundary-layer Theory*, 8th ed., Springer, Berlin, Germany, 2000.
 [5] CFD Online; 2016. [Online] (<http://www.cfd-online.com>)
 [6] H.K. Versteeg, W. Malalasekera, *An introduction to Computational Fluid Dynamics: The Finite Volume Method*, 2nd ed., Pearson Education Limited, Harlow, England, 2007.
 [7] M.V. Zagarola, *Mean-Flow Scaling of Turbulent Pipe Flow*, Princeton University, Princeton, New Jersey, USA, 1996.
 [8] M.V. Zagarola, A.J. Smits, Scaling of the mean velocity profile for turbulent pipe flow, *Phys. Rev. Lett.* 78 (1997) 239–242.
 [9] M.V. Zagarola, A.J. Smits, Mean-flow scaling of turbulent pipe flow, *J. Fluid Mech.* 373 (1998) 33–79.
 [10] B.J. McKeon, J. Li, W. Jiang, J.F. Morrison, A.J. Smits, Further observations on the mean velocity distribution in fully developed pipe flow, *J. Fluid Mech.* 501 (2004)

135–147.
 [11] Princeton Superpipe; 2016. [Online] (<https://smits.princeton.edu/superpipe-pitot-data/>)
 [12] K. Gersten, Fully developed turbulent pipe flow, in: W. Merzkirch (Ed.) *Fluid Mechanics of Flow Metering*, Springer, Berlin, Germany, 2005.
 [13] ANSYS CFX Reference Guide, Release 15.0, 2013.
 [14] ANSYS CFX-solver Theory Guide, Release 15.0, 2013.
 [15] F.R. Menter, Two-equation eddy-viscosity turbulence models for engineering applications, *AIAA J.* 32 (1994) 1598–1605.
 [16] FR. Menter, M. Kuntz, R. Langtry, Ten years of industrial experience with the SST turbulence model, in: K. Hanjalic, Y. Nagano, M. Tummers (Eds.), *Turbulence, Heat and Mass Transfer 4*, Begell House, New York, USA, 2003.
 [17] ANSYS CFX-solver Modeling Guide, Release 15.0, 2013.
 [18] M. Hultmark, M. Vallikivi, S.C.C. Bailey, A.J. Smits, Turbulent pipe flow at extreme Reynolds numbers, *Phys. Rev. Lett.* 108 (2012) 094501.
 [19] M. Hultmark, M. Vallikivi, S.C.C. Bailey, A.J. Smits, Logarithmic scaling of turbulence in smooth- and rough-wall pipe flow, *J. Fluid Mech.* 728 (2013) 376–395.
 [20] Princeton Superpipe; 2016. [Online] (<https://smits.princeton.edu/superpipe-turbulence-data/>)
 [21] N.P. Basse, P.K. Michelsen, S. Zoletnik, M. Saffman, M. Enderl, M. Hirsch, Spatial distribution of turbulence in the Wendelstein 7-AS stellarator, *Plasma Sources Sci. Technol.* 11 (2002) A138–A142.